Microstructural Feature and Magnetocaloric Effect of Mn$_{50}$Ni$_{40.5}$In$_{9.5}$ Melt-Spun Ribbons

Yiqiao Yang [1,2], **Zongbin Li** [1,*] (ID), **Zhenzhuang Li** [1], **Jiajing Yang** [1], **Bo Yang** [1], **Yu Dong** [1,2], **Haile Yan** [1], **Yudong Zhang** [3,4], **Claude Esling** [3,4], **Xiang Zhao** [1,*] and **Liang Zuo** [1,5] (ID)

[1] Key Laboratory for Anisotropy and Texture of Materials (Ministry of Education), School of Material Science and Engineering, Northeastern University, Shenyang 110819, China; yangyq@mail.neu.edu.cn (Y.Y.); li_zhenzhuang@yeah.net (Z.L.); yjj02030222@163.com (J.Y.); yangb@atm.neu.edu.cn (B.Y.); dongy@mail.neu.edu.cn (Y.D.); yanhaile@mail.neu.edu.cn (H.Y.); lzuo@mail.neu.edu.cn (L.Z.)

[2] Research Institute, Northeastern University, Shenyang 110819, China

[3] Laboratoire d'Étude des Microstructures et de Mécanique des Matériaux (LEM3), CNRS UMR 7239, Université de Lorraine, 57045 Metz, France; yudong.zhang@univ-lorraine.fr (Y.Z.); claude.esling@univ-lorraine.fr (C.E.)

[4] Laboratory of Excellence on Design of Alloy Metals for low-mAss Structures (DAMAS), Université de Lorraine, 57045 Metz, France

[5] Taiyuan University of Science and Technology, Taiyuan 030024, China

* Correspondence: lizongbin@126.com (Z.L.), zhaox@mail.neu.edu.cn (X.Z.)

Abstract: The microstructure and magnetocaloric properties of the melt-spun and annealed Mn$_{50}$Ni$_{40.5}$In$_{9.5}$ ribbons were studied. It is shown that the post-annealing results in a considerable increase of the grain size for the initial austenite, where the columnar-shaped austenite grains almost run through the whole ribbon. Both the melt-spun and annealed ribbons consist of the mixture of austenite and martensite at room temperature, where a 8-layered modulated (8M) martensite structure was identified through selected area electron diffraction (SAED). Further High-angle Annular Dark-field (HAADF) characterizations reveal that the modulation period of 8M martensite is not homogeneous in one martensite plate. Due to strong magneto-structural coupling, the inverse martensitic transformation from a weak magnetic martensite to a strong magnetic austenite can be induced by the magnetic field, resulting in the inverse magnetocaloric effect around room temperature. For a field change of 5 T, the magnetic entropy change ΔS_M of 3.7 J·kg^{-1}·K^{-1} and 6.1 J·kg^{-1}·K^{-1}, and the effective refrigerant capacity RC_{eff} of 52.91 J·kg^{-1} and 99.08 J·kg^{-1} were obtained for melt-spun and annealed ribbons, respectively. The improvement of the magnetocaloric properties after annealing should be attributed to the enhanced atomic ordering and magnetization difference between two phases, as well as the reduced hysteresis loss. In addition, both the melt-spun and annealed ribbons can work at a relatively wide temperature range, i.e., δT_{FWHM} = 34 K for melt-spun ribbons and δT_{FWHM} = 28 K for annealed ribbons.

Keywords: Mn-Ni-In ribbons; microstructure; magnetostructural transformation; magnetocaloric effect

1. Introduction

The magnetocaloric effect (MCE), referring to the isothermal magnetic entropy change (ΔS_M) or the adiabatic temperature variation (ΔT_{ad}), is an intrinsic magneto-thermal phenomena of magnetic materials when a magnetic field is applied or removed. Based on the MCE, the magnetic refrigeration is a recently developed novel solid-state cooling technology [1–4]. Compared to the conventional vapour compression/expansion system, the magnetic refrigeration is high-efficient and

environment-friendly [4]. Currently, there is intensive research interest on the study of materials with giant MCE near room temperature.

Ni-Mn-X (X = In, Sn, Sb)-based Heusler-type alloys are recently developed novel multi-functional materials. Upon the application of an external magnetic field, these alloys can exhibit significant field-controlled functional behaviours, such as magnetic shape memory effect [5,6], magnetocaloric effect [2,7] and magnetoresistance effect [8], owing to the field-induced inverse martensitic transformation from a weak magnetic martensite to a ferromagnetic austenite [5,7], i.e., magnetostructural transformation. It is known that Mn atoms in NiMn-based Heusler alloys make the highest contribution to the magnetization. Thus, proper modification of the composition, especially the content of Mn, may enlarge the magnetization difference ΔM between high-temperature austenite and low-temperature martensite, and consequently, result in the enhancement of magnetostructural coupling and improvement of their field-controlled functional behaviours. In this regard, the exploration of Mn-rich MnNi-based alloys has aroused great interest [9–15].

Sánchez Llamazares et al. reported that $Mn_{50}Ni_{40}In_{10}$ melt-spun ribbons can undergo the martensitic transformation on cooling and such transformation was found to be from cubic austenite to monoclinic 14-layered modulated (14M) martensite based on X-ray diffraction (XRD) measurements [15]. Similar transformation behaviour was also found in $Mn_{49}Ni_{41}In_9$ melt-spun ribbons [9]. Xuan et al. reported that the phase transformation temperatures of Mn-Ni-In alloys were strongly dependent on the composition and they decreased with the increase of In content [11]. Hernando et al. [12] illustrated that Mn-Ni-In alloys can exhibit significant MCE and a maximum ΔS_M ($\Delta S_M{}^{Max}$) of 3.6 $J \cdot kg^{-1} \cdot K^{-1}$ can be achieved under the field change of 3 T around 230 K in $Mn_{50}Ni_{40}In_{10}$ melt-spun ribbons. Ren et al. prepared the $Mn_{50}Ni_{40}In_{10}$ alloy through directional solidification and an enhanced $\Delta S_M{}^{Max}$ up to 10.7 $J \cdot kg^{-1} \cdot K^{-1}$ was achieved under the field change of 3 T around 245 K, due to the enlarged grain size in directionally solidified alloy [13].

In general, the martensite in Heusler-type alloys usually exhibits the long-period modulated crystal structure. The type of modulated structure appears to be easy to distinguish through selected area electron diffraction (SAED) patterns owing to the existence of extra spots between two main spots [16]. However, because Mn-Ni-In-based alloys are developed very recently, there still lacks further confirmation on the above-mentioned 14M structure through SAED. On the other hand, the reported temperature window of MCE for Mn-Ni-In alloys is still well below room temperature [12,13], which imposes a strong challenge on the room temperature applications. In addition, the working temperature range (i.e., δT_{FWHM}, the full width at half maximum of the ΔS_M curve) is still relatively narrow for Mn-Ni-In alloys [13], which is unfavourable for the practical application. For example, the δT_{FWHM} for the directionally solidified $Mn_{50}Ni_{40}In_{10}$ alloy was ~16 K [13]. As known, the magnetic refrigeration applications require not only a significant ΔS_M but also a wide working temperature interval of MCE. Apparently, the development of magnetic materials with large MCE as well as the wide working temperature range is of great significance for the magnetic refrigeration applications.

It is worth mentioning that the melt-spinning technique has been well developed for the fabrication of NiMn-based alloys, where a highly homogeneous chemical composition can be achieved without resorting to long-time high-temperature post-heat treatments. Besides, such method offers an ideal geometrical shape of refrigerants since the influence of the demagnetizing field on the ΔS_M could be minimized when ribbon-shaped refrigerants are magnetized along their longitudinal direction [17].

In this work, in order to tune the martensitic transformation around room temperature, Mn-rich Mn-Ni-In ribbons with a modified composition of $Mn_{50}Ni_{40.5}In_{9.5}$ were prepared by melt-spinning and then annealed at 1073 K for 5 min. Based on SAED, a 8-layered modulated (8M) martensite structure was revealed in ribbons. Furthermore, it was clarified by High-angle Annular Dark-field (HAADF) characterizations that the modulation period of 8M martensite was not homogeneous in single martensite plate. In addition, due to the strong magneto-structural coupling, the ribbons exhibit the field-induced inverse martensitic transformation behavior, resulting in the inverse magnetocaloric

effect. It was shown that both melt-spun and annealed ribbons can work in a relatively wide temperature range, i.e., δT_{FWHM} = 34 K for melt-spun ribbons and δT_{FWHM} = 28 K for annealed ribbons.

2. Experimental

The master polycrystalline alloy with the nominal composition of $Mn_{50}Ni_{40.5}In_{9.5}$ (at. %) was prepared by means of arc-melting under the protection of argon atmosphere. The ribbon samples were prepared by melt-spinning also under argon atmosphere, where the rotation speed of copper wheel was set to be 20 m/s. Several pieces of ribbon sample were further annealed at 1073 K in argon atmosphere for 5 min, and then they were quenched into ice water. For the microstructural observations in scanning electron microscope (SEM), the ribbon plane was electrolytically polished by using a solution of 20% nitric acid in methanol. For transmission electron microscope (TEM) observations, the samples were electrolytically thinned in a twin-jet device with the same solution mentioned above.

The composition of the ribbons was verified by Electron Probe Micro-Analysis (EPMA). The actual compositions for melt-spun and annealed ribbons were determined to be $Mn_{50.1}Ni_{40.3}In_{9.6}$ and $Mn_{49.8}Ni_{40.7}In_{9.5}$, respectively, with the uncertainties of $\pm 0.2\%$. The martensitic transformation temperatures were determined by differential scanning calorimetry (DSC), where the heating/cooling rate was 10 K/min. The crystal structure was identified by means of X-ray diffraction (XRD) using Cu-$K\alpha$ radiation and selected area electronic diffraction (SAED) at room temperature. The microstructural observations were carried out by SEM (Jeol JSM 7001F) and TEM (JEM-ARM 200F). The magnetic properties were characterized by the physical property measuring system (PPMS-9T, Quantum Design). In order to minimize the demagnetization influence, the magnetic field was applied along the ribbon length direction (rolling direction) during measurements. The thermal-magnetic (M–T) curves were measured at a heating and cooling rate of 2.5 K/min.

3. Results and Discussion

3.1. Martensitic Transformation

Figure 1 displays the DSC curves for the melt-spun and annealed $Mn_{50}Ni_{40.5}In_{9.5}$ ribbons. Large exothermic and endothermic peaks can be clearly observed between 250 K and 350 K, indicating that the samples underwent reversible martensitic transformation. According to the DSC curves, the start and finish temperatures for the forward transformation (M_s, M_f) and the inverse transformation (A_s, A_f) were well determined, as shown in Table 1. The martensitic transformation temperatures of both melt-spun and annealed ribbons are around room temperature. Moreover, the post-annealing results in certain increase of the martensitic transformation temperatures, which should be attributed to the reduction of crystal defects, the enhancement of atomic ordering and the relaxation of internal stresses after annealing [18–21]. In addition, the post-annealing can also result in a reduced transformation hysteresis (calculated by $(A_s + A_f - M_s - M_f)/2$) in annealed ribbons (~23 K) with respect to melt-spun ribbons (~30.5 K).
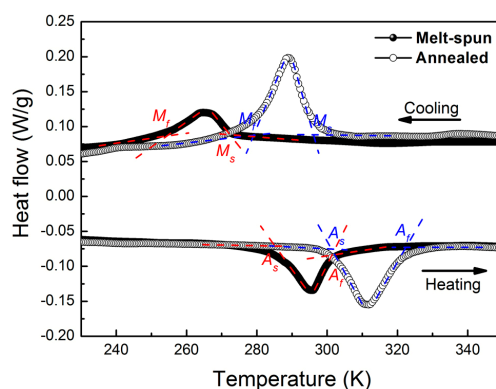

Figure 1. Differential scanning calorimetry (DSC) curves for melt-spun and annealed $Mn_{50}Ni_{40.5}In_{9.5}$ ribbons.

Table 1. Martensitic transformation temperatures (M_s, M_f, A_s, A_f) for melt-spun and annealed $Mn_{50}Ni_{40.5}In_{9.5}$ ribbons.

Ribbons	M_s (K)	M_f (K)	A_s (K)	A_f (K)
Melt-spun	272	254	285	302
Annealed	297	279	301	321

3.2. Crystal Structure

To analyze the crystal structure of the ribbons, XRD measurements were performed. Figure 2a shows the room temperature XRD patterns measured on the ribbon plane for both melt-spun and annealed ribbons. It is shown that both melt-spun and annealed ribbons consist of the mixture of austenite and martensite at room temperature. For the melt-spun ribbons, some minor peaks belonging to martensite around $\{2\,2\,0\}_A$ peak were identified, as illustrated in the inset of Figure 2a for 2θ range from 40° to 46°. For the annealed ribbons, the intensity of martensite peaks is obviously higher than that of melt-spun ribbons, indicating the increase of volume fraction of martensite and the enhanced martensitic transformation temperature after annealing. Moreover, the lattice constant of the cubic austenite for the annealed ribbons (a_A = 5.974 Å) is slightly smaller than that of melt-spun ribbons (a_A = 5.991 Å), which should be attributed to the reduced lattice defects in the annealed ribbons [19].
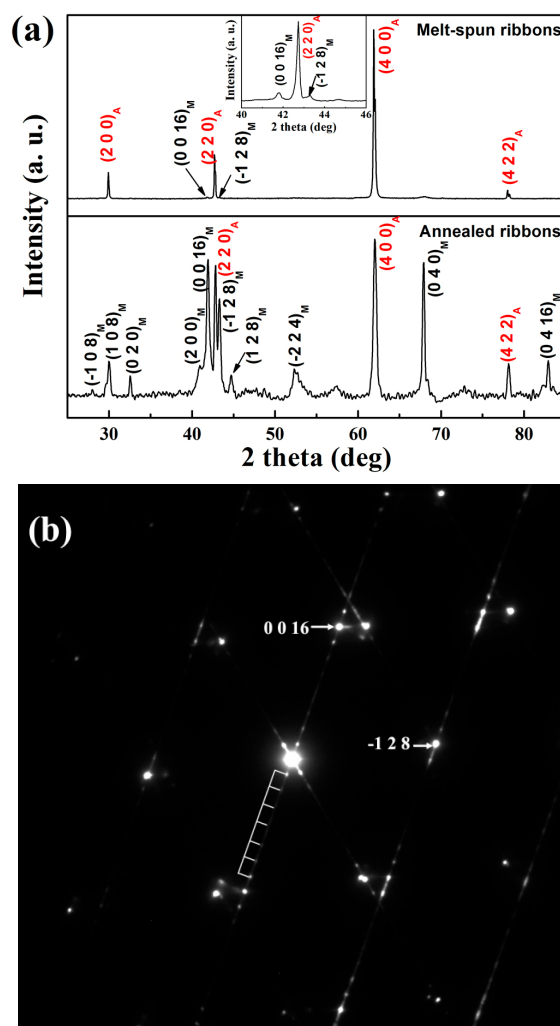
Figure 2. (**a**) X-ray diffraction patterns for melt-spun and annealed ribbons. (**b**) Selected area electronic diffraction (SAED) pattern for the martensite of melt-spun ribbons along <2 1 0>$_M$.

It is worth noting that several diffraction peaks of martensite appear around {2 2 0}$_A$ peak in the XRD patterns in the 2θ range from 40° to 46°, suggesting that the martensite in the ribbons could be modulated type. In order to further figure out the lattice modulation information on the martensite, SAED was performed on the melt-spun ribbons. A typical SAED pattern along <2 1 0>$_M$ for two martensite plates with type I twin relation was shown in Figure 2b. It is found that the intensity of the satellite spots is quite weak with slight elongation and even dispersed. Generally, seven satellite spots are located between two main spots, suggesting that the martensite in the present ribbons should be 8-layered modulated (8M) martensite with monoclinic structure [22]. Based on this crystal structure model, the lattice constants of 8M martensite in melt-spun ribbons were determined to be a_M = 4.540 Å, b_M = 5.659 Å, c_M = 35.96 Å, β = 94.4°. In addition, the volume fraction of austenite was determined to be 96.6% and the martensite to be 3.4% through fitting the XRD pattern.

3.3. Microstructure

Figure 3a shows a typical room temperature backscattered electron (BSE) image of the ribbon plane for the melt-spun ribbons. The martensite is in plate shape and located in the initial austenite grains. Some residual austenite with dark contrast can be identified, which is consistent with XRD measurements. Since the melt-spinning is a rapid solidification process, it provides an ultra-high solidification rate. Thus, the grain size of initial austenite is greatly refined. In general, the grain size of initial austenite grains in melt-spun ribbons is about 10 μm. Figure 3b shows the secondary electron (SE) image taken from the cross-section that is perpendicular to the ribbon plane for the melt-spun ribbons. It is shown that the initial austenite grains of melt-spun ribbons are in columnar shape, growing approximately along the ribbon plane normal. Moreover, the grain size at wheel-side is much smaller than that of air-side. This morphological feature should be caused by the specific heat transfer condition during the melt-spun process. As expected, the cooling rate at wheel-side is higher than that of air-side, resulting in the refined grain size at wheel-side.
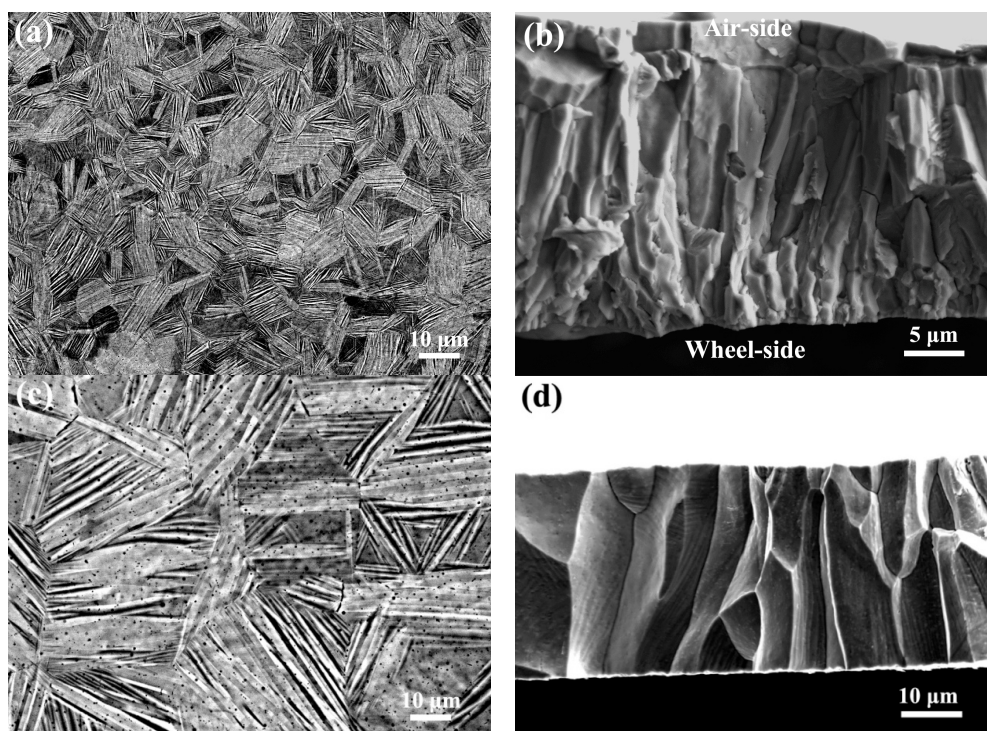

Figure 3. (**a**) Backscattered electron (BSE) image of the ribbon plane for melt-spun ribbons; (**b**) Secondary electron (SE) image of cross-section for melt-spun ribbons; (**c**) BSE image of ribbon plane for annealed ribbons; (**d**) SE image of cross-section for annealed ribbons.

Figure 3c shows the BSE image of the ribbon plane for the annealed ribbons. As compared to the melt-spun ribbons, the grain size of the initial austenite (~40 μm) has been greatly increased after annealing. In the figure, the black dots could be due to the falling particles during the electrolytical polishing process. In addition, the columnar-shaped initial austenite grains in annealed ribbons almost run through the whole ribbon thickness, as shown in Figure 3d. Such morphological feature would result in a great reduction of grain boundary amount. Therefore, the transformation resistance in annealed ribbons should be significantly reduced, which should be responsible for the decrease of transformation hysteresis in annealed ribbons. On the other hand, the grain boundaries are composed of atoms with disorder arrangement. Thus, the existence of a large amount of grain boundaries should decrease the atomic ordering. From this point, the reduction of grain boundaries should be beneficial for the enhancement of the atomic ordering. After the annealing, the grain size of the ribbons is greatly increased and the grain boundary amount is significantly decreased, resulting in the enhancement of the atomic ordering.

Figure 4a shows a typical TEM bright-field image of the martensite plates for the melt-spun ribbons. Locally, the martensite plates are bordered by the inter-plate interfaces. There exists a large amount of stacking faults inside the martensite plates, which is similar to the modulated martensite in NiMn-based alloys [23–25]. Locally, four types of martensite variants (represented as A, B, C and D in Figure 4a) are distributed alternately, which is in agreement with the 7M martensite with monoclinic structure in Ni-Mn-Ga alloys [25,26].
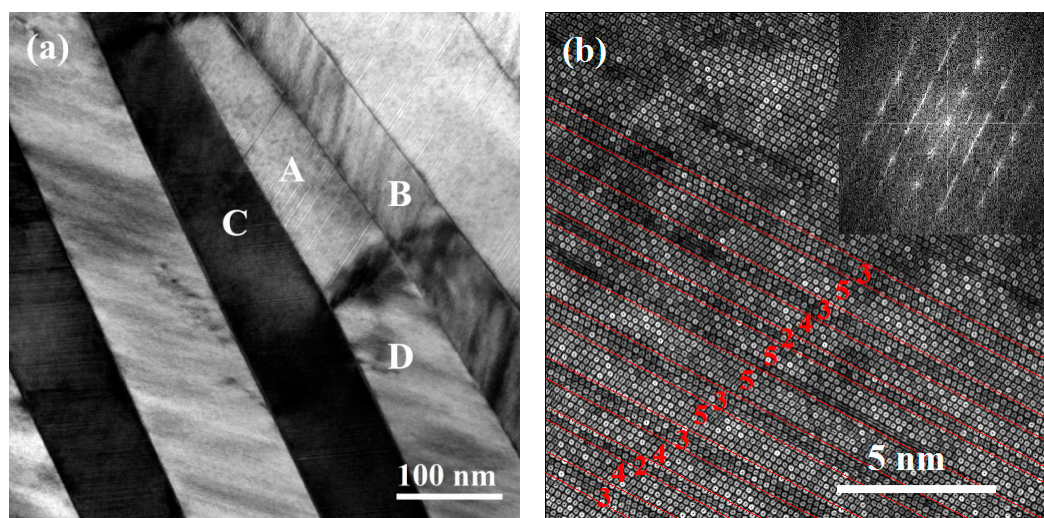

Figure 4. (**a**) TEM bright-field image of modulated martensite plates. (**b**) High-angle Annular Dark-field (HAADF) atomic image along <0 1 0>$_M$ in one martensite plate of melt-spun ribbons.

In order to get further insight into the microstructural feature of martensite, Scanning Transmission Electron Microscopy (STEM) observations were performed. A High-angle Annular Dark-field (HAADF) image acquired from one martensite plate of melt-spun ribbons along <0 1 0>$_M$ axis is presented in Figure 4b. The inset shows the corresponding Fast Fourier Transformation (FFT) pattern. It is noted that the modulation period is not homogeneous and there exist several kinds of modulation period, as indicated in the figure. Such inhomogeneity of the modulation period could be the reason that accounts for the elongation of the satellite spots in Figure 2b. Thus, the 8M structure could be a global average structure.

3.4. Magnetocaloric Effects

Figure 5a,b present temperature dependence of magnetization (M–T curves) obtained under the field of 0.005 T and 5 T for melt-spun and annealed ribbons, respectively. From the M–T curves under

the low field of 0.005 T (Figure 5a), it is shown that the paramagnetic-to-ferromagnetic transition occurs at ~329 K (T_C), followed by the martensitic transformation with certain thermal hysteresis of 30 K. This confirms the nature of first-order transformation. In contrast, no obvious thermal hysteresis is observed for the second-order magnetic transition. For the annealed ribbons (Figure 5b), the low field M–T curves present the similar characteristic to those of melt-spun ribbons, but with enhanced martensitic transformation temperatures and T_C (~333 K).
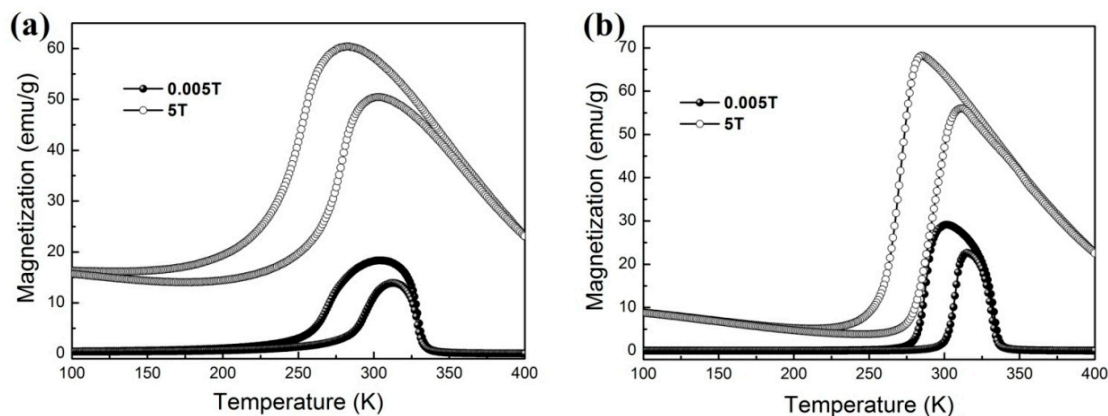

Figure 5. (**a**) Thermo-magnetic (M–T) curves measured under the field of 0.005 T and 5 T for melt-spun ribbons. (**b**) M–T curves measured under the field of 0.005 T and 5 T for annealed ribbons.

According to the M–T curves measured under the field of 5 T, it is seen that for both melt-spun and annealed ribbons, the martensitic transformation is accompanied by the large magnetization difference, i.e., a magnetostructural transformation from ferromagnetic austenite to weak magnetic martensite. Moreover, the application of field can significantly decrease the martensitic transformation temperatures. The A_s of melt-spun ribbons is reduced by ~20 K under the field of 5 T when compared to that under low magnetic field of 0.005 T, with a rate of 4 K/T. Such phenomenon indicates that the field-induced inverse martensitic transformation can be expected. For the annealed ribbons, the field of 5 T can result in a reduction of ~24 K for A_s, with a rate of 4.8 K/T. Notably, the field dependence of transformation temperatures can be enhanced through post-annealing, which should be attributed to relatively higher magnetization difference between two phases as well as the reduced transformation resistance after annealing.

It is known that the influence of external magnetic field on the martensitic transformation temperatures can be well described by the Clausius–Clapeyron equation, i.e., $\Delta T/\Delta H = \Delta M/\Delta S$, where ΔS and ΔM represent the transformation entropy and the differences in magnetization between austenite and martensite, respectively. Here, for the melt-spun ribbons, the ΔS was determined to be 9.8 J·kg^{-1}·K^{-1} from the DSC measurements. According to the Clausius–Clapeyron equation, the field change of 5 T can result in the temperature change (ΔT) of 18.4 K, which is in agreement with the experimentally observed temperature shift (~20 K). For the annealed ribbons, the ΔS determined from the DSC measurements is 11.6 J·kg^{-1}·K^{-1}. The ΔT value was determined to be 22.4 K under the field change of 5 T according to Clausius–Clapeyron equation. This is also in agreement with the experimental result.

For the determination of the magnetic entropy change (ΔS_M), sets of isothermal magnetization (M–H) curves were measured across the inverse martensitic transformation for both melt-spun and annealed ribbons with the field up to 5 T, as shown in Figure 6a,b. In order to properly determine the ΔS_M values [27], the loop method was employed for the M–H measurements. Before each measurement, the sample was cooled to 150 K firstly under zero field to ensure a pure martensite, then the sample was heated under zero field to the target measurement temperature for the measurements. It is seen in Figure 6a,b that the ribbons exhibit the typical meta-magnetic behaviour for both melt-spun and

annealed ribbons [5]. At a certain critical field $\mu_0 H_{cr}$, a sudden magnetization change from weak magnetic martensite to ferromagnetic austenite can be observed in M–H curves.
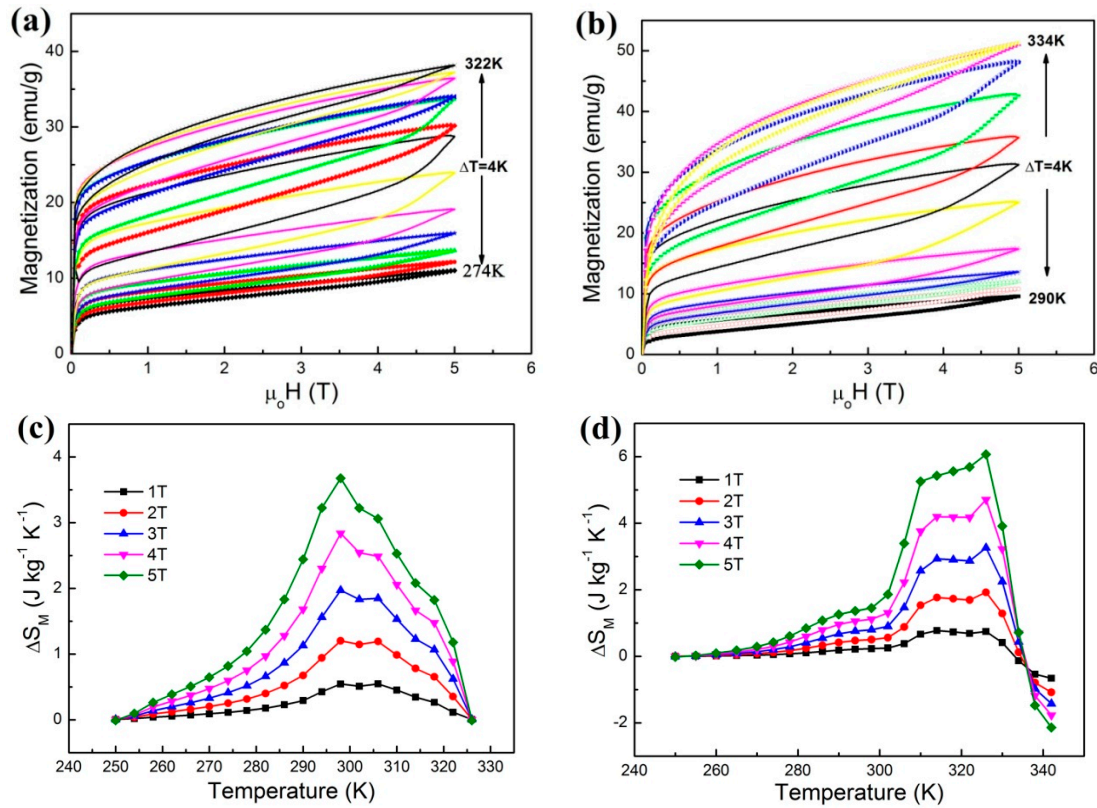

Figure 6. (**a**) Isothermal magnetization curves for the melt-spun ribbons; (**b**) Isothermal magnetization curves for the annealed ribbons; (**c**) ΔS_M as a function of temperature change under various field changes for melt-spun ribbons; (**d**) ΔS_M as a function of temperature change under various field changes for annealed ribbons.

Based on the measured isothermal magnetization curves, the magnetic entropy change (ΔS_M) was calculated according to the Maxwell relation, i.e., $\Delta S_M(T, H) = \mu_0 \int_0^H (\partial M / \partial T)_H dH$. The ΔS_M as a function of temperature change for the melt-spun and annealed ribbons at various field change is shown in Figure 6c,d, respectively. The ribbons exhibit the positive magnetic entropy change, i.e., inverse magnetocaloric effect, which is consistent with the transformation from weak magnetic martensite to ferromagnetic austenite. Under the field change of 5 T, the maximum ΔS_M of 3.7 J·kg^{-1}·K^{-1} and 6.1 J·kg^{-1}·K^{-1} for melt-spun and annealed ribbons was obtained, respectively, due to the abrupt magnetization changes in the vicinity of the inverse martensitic transformation. Noted that ΔS_M curves of the annealed ribbons exhibit a plateau and such plateau covers a broad temperature span under the field change of 5 T, i.e., from 310 K to 326 K, which should be quite beneficial for the practical applications in a relatively wider temperature range. The maximum ΔS_M (6.1 J·kg^{-1}·K^{-1} for $\mu_0 \Delta H = 5$ T) for the annealed $Mn_{50}Ni_{40.5}In_{9.5}$ ribbons is relatively smaller than that of melt-spun $Mn_{50}Ni_{41}In_9$ ribbons (5.7 J·kg^{-1}·K^{-1} for $\mu_0 \Delta H = 3$ T) [9]. This could be due to the slight difference in composition and the resultant phase transformation temperatures. In addition, the temperature protocol for the measurement of M–H curves could also exert a strong influence on the determination of ΔS_M according to the Maxwell relation. It has been reported in literature that two methods [28], i.e., discontinuous heating and continuous heating, can be performed for M–H measurements. As mentioned before, a loop method (discontinuous heating protocol) was employed for the M–H measurements in the present work. On the other hand, the M–H curves were measured through

continuous heating protocol for melt-spun $Mn_{50}Ni_{41}In_9$ ribbons [9], as deduced from the shape of M–H curves. It has been revealed that the continuous heating method would result in a relatively higher ΔS_M with respect to that from the discontinuous heating method [28], due to the existence of residual field-induced austenite.

Another important parameter to evaluate MCE is the refrigeration capacity (*RC*). *RC* values can be determined by the equation $RC = \int_{T_{cold}}^{T_{hot}} \Delta S_M dT$, where T_{cold} and T_{hot} are the corresponding temperatures at full width half maximum of the ΔS_M peak. For $\mu_0 \Delta H = 5$ T, the *RC* values for the melt-spun and annealed ribbon are calculated to be 80.5 J·kg^{-1} and 126.6 J·kg^{-1}, respectively. The *RC* value of annealed ribbons is obviously higher than of melt-spun ribbons, which should be attributed to the appearance of plateau in the ΔS_M curves. In addition, the present *RC* value in annealed ribbons is higher than that of $Mn_{50}Ni_{40}Sn_{10}$ melt-spun ribbons (*RC* = 113.3 J·kg^{-1}, $\mu_0 \Delta H = 5$ T) [29].

In order to determine the effective refrigeration capacity (*RC*$_{eff}$), the hysteresis loss should be taken into account. The hysteresis losses at different temperatures are determined by calculating the enclosed area between field-up and field-down magnetization curves. Under the field change of 5 T, the average hysteretic losses of melt-spun and annealed ribbons are calculated to be 27.55 J·kg^{-1} and 31.54 J·kg^{-1}, which are much lower than that of directionally solidified $Mn_{50}Ni_{40}In_{10}$ alloy (53.06 J·kg^{-1}, $\mu_0 \Delta H = 3$ T) [13]. After subtracting the average hysteresis losses, the effective refrigerant capacity *RC*$_{eff}$ under the field change of 5 T were determined to be 52.91 J·kg^{-1} and 99.08 J·kg^{-1} for melt-spun and annealed ribbons, respectively. Apparently, the magnetocaloric properties of ribbons were greatly improved after annealing, which should be attributed to the enhanced atomic ordering and magnetization difference between two phases, as well as the reduced hysteresis loss. Moreover, the present *RC*$_{eff}$ value in annealed $Mn_{50}Ni_{40.5}In_{9.5}$ ribbons is also larger than that of $Mn_{50}Ni_{40}Sn_{10}$ melt-spun ribbons (*RC*$_{eff}$ = 72.9 J·kg^{-1}) [29].

It is noted that the full width at half-maximum of the ΔS_M curve, i.e., $\delta T_{FWHM} = T_{hot} - T_{cold}$, that indicates the working temperature range, for the present ribbons covers a relatively wide temperature range, i.e., $\delta T_{FWHM} = 34$ K for melt-spun ribbons (284 K to 318 K) and $\delta T_{FWHM} = 28$ K for annealed ribbons (303 K to 331 K), which is much higher than the corresponding value of directionally solidified $Mn_{50}Ni_{40}In_{10}$ alloy (i.e., 16 K) [13]. Apparently, the widened δT_{FWHM} would give positive contribution to the refrigeration capacity as well as work temperature range. By combination of melt-spun and annealed ribbons, the work temperature range of $Mn_{50}Ni_{40.5}In_{9.5}$ ribbons can cover 47 K (284 K to 331 K).

4. Summary

In summary, the microstructure, magnetostructural transformation and magnetocaloric properties of melt-spun and annealed $Mn_{50}Ni_{40.5}In_{9.5}$ ribbons were studied. It is shown that the post-annealing can increase the martensitic transformation temperature and grain size, but decrease the transformation hysteresis. Both melt-spun and annealed ribbons consist of the mixture of austenite and 8M martensite at room temperature. Based on HAADF, it is revealed that the 8M martensite can exhibit several kinds of modulation period in one martensite plate. Owing to the large magnetization difference, the magnetic field can greatly reduce the martensitic transformation temperatures in both melt-spun and annealed ribbons, resulting in the occurrence of field-induced inverse martensitic transformation. Under the field change of 5 T, the maximum ΔS_M for melt-spun and annealed ribbons were determined to be 3.7 J·kg^{-1}·K^{-1} and 6.1 J·kg^{-1}·K^{-1}, and the effective refrigerant capacity *RC*$_{eff}$ 52.91 J·kg^{-1} and 99.08 J·kg^{-1}, respectively. The property improvement for the annealed ribbons should be attributed to the enhanced atomic ordering and magnetization difference between two phases, as well as the reduced hysteresis loss. Moreover, both melt-spun and annealed ribbons can work in a relatively wide temperature range, i.e., $\delta T_{FWHM} = 34$ K for melt-spun ribbons and $\delta T_{FWHM} = 28$ K for annealed ribbons.

References

1. Pecharsky, V.K.; Gschneidner, K.A., Jr. Magnetocaloric effect and magnetic refrigeration. *J. Magn. Magn. Mater.* **1999**, *200*, 44–56. [CrossRef]

2. Planes, A.; Mañosa, L.; Acet, M. Magnetocaloric effect and its relation to shape-memory properties in ferromagnetic Heusler alloys. *J. Phys. Condens. Matter* **2009**, *21*, 233201. [CrossRef] [PubMed]

3. Gutfleisch, O.; Willard, M.A.; Brück, E.; Chen, C.H.; Sankar, S.G.; Liu, J.P. Magnetic materials and devices for the 21st century: Stronger, lighter, and more energy efficient. *Adv. Mater.* **2011**, *23*, 821–842. [CrossRef] [PubMed]

4. Yu, B.F.; Gao, Q.; Zhang, B.; Meng, X.Z.; Chen, Z. Review on research of room temperature magnetic refrigeration. *Int. J. Refrig.* **2003**, *26*, 622–636. [CrossRef]

5. Kainuma, R.; Imano, Y.; Ito, W.; Sutou, Y.; Morito, H.; Okamoto, S.; Kitakami, O.; Oikawa, K.; Fujita, A.; Kanomata, T.; et al. Magnetic-field-induced shape recovery by reverse phase transformation. *Nature* **2006**, *439*, 957–960. [CrossRef] [PubMed]

6. Kainuma, R.; Imano, Y.; Ito, W.; Morito, H.; Sutou, Y.; Oikawa, K.; Fujita, A.; Ishida, K.; Okamoto, S.; Kitakami, O.; et al. Metamagnetic shape memory effect in a Heusler-type $Ni_{43}Co_7Mn_{39}Sn_{11}$ polycrystalline alloy. *Appl. Phys. Lett.* **2006**, *88*, 192513. [CrossRef]

7. Liu, J.; Gottschall, T.; Skokov, K.P.; Moore, J.D.; Gutfleisch, O. Giant magnetocaloric effect driven by structural transitions. *Nat. Mater.* **2012**, *11*, 620–626. [CrossRef] [PubMed]

8. Yu, S.Y.; Liu, Z.H.; Liu, G.D.; Chen, J.L.; Cao, Z.X.; Wu, G.H.; Zhang, B.; Zhang, X.X. Large magnetoresistance in single-crystalline $Ni_{50}Mn_{50-x}In_x$ alloys (x = 14–16) upon martensitic transformation. *Appl. Phys. Lett.* **2006**, *89*, 162503. [CrossRef]

9. Li, H.; Feng, S.; Ren, J.; Zhai, Q.; Fu, J.; Luo, Z.; Zheng, H. Magnetostructural transitions in Mn-rich Heusler Mn–Ni–In melt-spun ribbons with enhanced magnetocaloric effect. *J. Magn. Magn. Mater.* **2015**, *391*, 17–21. [CrossRef]

10. Sánchez Llamazares, J.L.; Hernando, B.; Prida, V.M.; García, C.; González, J.; Varga, R.; Ross, C.A. Magnetic field influence on the structural transformation in ferromagnetic shape memory alloy $Mn_{50}Ni_{40}In_{10}$ melt spun ribbons. *J. Appl. Phys.* **2009**, *105*, 07A945. [CrossRef]

11. Xuan, H.C.; Ma, S.C.; Cao, Q.Q.; Wang, D.H.; Du, Y.W. Martensitic transformation and magnetic properties in high-Mn content $Mn_{50}Ni_{50-x}In_x$ ferromagnetic shape memory alloys. *J. Alloys Compd.* **2011**, *509*, 5761–5764. [CrossRef]

12. Hernando, B.; SanchezLlamazares, J.L.; Prida, V.M.; Baldomir, D.; Serantes, D.; Ilyn, M.; González, J. Magnetocaloric effect in preferentially textured $Mn_{50}Ni_{40}In_{10}$ melt spun ribbons. *Appl. Phys. Lett.* **2009**, *94*, 222502. [CrossRef]

13. Ren, J.; Li, H.W.; Feng, S.T.; Zhai, Q.J.; Fu, J.X.; Luo, Z.P.; Zheng, H.X. Giant magnetocaloric effect in a Heusler $Mn_{50}Ni_{40}In_{10}$ unidirectional crystal. *Intermetallics* **2015**, *65*, 10–14. [CrossRef]

14. Ren, J.; Tong, S.T.; Fang, Y.; Zhai, Q.J.; Luo, Z.P.; Zheng, H.X. Enhanced magnetocaloric effect in a Co-doped Heusler $Mn_{50}Ni_{37}Co_3In_{10}$ unidirectional crystal. *J. Phys. Chem. Solids* **2016**, *98*, 233–236. [CrossRef]

15. SánchezLlamazares, J.L.; Sanchez, T.; Santos, J.D.; Pérez, M.J.; Sanchez, M.L.; Hernando., B. Martensitic phase transformation in rapidly solidified $Mn_{50}Ni_{40}In_{10}$ alloy ribbons. *Appl. Phys. Lett.* **2008**, *92*, 012513.

16. Pons, J.; Chernenko, V.A.; Santamarta, R.; Cesari, E. Crystal structure of martensitic phases in Ni-Mn-Ga shape memory alloys. *Acta Mater.* **2000**, *48*, 3027–3038. [CrossRef]

17. Caballero-Flores, R.; Franco, V.; Conde, A.; Kiss, L.F. Influence of the demagnetizing field on the determination of the magnetocaloric effect from magnetization curves. *J. Appl. Phys.* **2009**, *105*, 07A919. [CrossRef]

18. Ma, S.C.; Cao, Q.Q.; Xuan, H.C.; Zhang, C.L.; Shen, L.J.; Wang, D.H. Magnetic and magnetocaloric properties in melt-spun and annealed $Ni_{42.7}Mn_{40.8}Co_{5.2}Sn_{11.3}$ ribbons. *J. Alloys Compd.* **2011**, *509*, 1111–1114. [CrossRef]

19. Chernenko, V.A.; Cesari, E.; Pons, J.; Seguí, C. Phase transformations in rapidly quenched Ni-Mn-Ga alloys. *J. Mater. Res.* **2000**, *15*, 1496–1504. [CrossRef]

20. Liu, J.; Scheerbaum, N.; Hinz, D.; Gutfleisch, O. Magnetostructural transformation in Ni-Mn-In-Co ribbons. *Appl. Phys. Lett.* **2008**, *92*, 162509. [CrossRef]

21. Cai, W.; Feng, Y.; Sui, J.H.; Gao, Z.Y.; Dong, G.F. Microstructure and martensitic phase transformation behavior of the $Ni_{50}Mn_{36}In_{14}$ melt-spun ribbons. *Scr. Mater.* **2008**, *58*, 830–833. [CrossRef]

22. Chernenko, V.A.; Seguí, C.; Cesari, E.; Pons, J.; Kokorin, V.V. Sequence of martensitic transformations in Ni-Mn-Ga alloys. *Phys. Rev. B* **1998**, *57*, 2659–2662. [CrossRef]

23. Sutou, Y.; Imano, Y.; Koeda, N.; Omori, T.; Kainuma, R.; Ishida, K.; Oikawa, K. Magnetic and martensitic transformations of NiMnX (X=In,Sn,Sb) ferromagnetic shape memory alloys. *Appl. Phys. Lett.* **2004**, *85*, 4358–4360. [CrossRef]

24. Nishida, M.; Hara, T.; Matsuda, M.; Ii, S. Crystallography and morphology of various interfaces in Ti-Ni, Ti-Pd and Ni-Mn-Ga shape memory alloys. *Mater. Sci. Eng. A* **2008**, *481*, 18–27. [CrossRef]

25. Li, Z.B.; Yang, B.; Zhang, Y.D.; Esling, C.; Zou, N.F.; Zhao, X.; Zuo, L. Crystallographic insights into the intermartensitic transformation in Ni-Mn-Ga alloys. *Acta Mater.* **2014**, *74*, 9–17. [CrossRef]

26. Li, Z.B.; Zhang, Y.D.; Esling, C.; Zhao, X.; Zuo, L. Determination of the orientation relationship between austenite and incommensurate 7M modulated martensite in Ni-Mn-Ga alloys. *Acta Mater.* **2011**, *59*, 2762–2772. [CrossRef]

27. Quintana-Nedelcos, A.; Sánchez Llamazares, J.L.; Sánchez-Valdés, C.F.; Álvarez Alonso, P.; Gorria, P.; Shamba, P.; Morley, N.A. On the correct estimation of the magnetic entropy change across the magneto-structural transition from the Maxwell relation: Study of $MnCoGeB_x$ alloy ribbons. *J. Alloys Compd.* **2017**, *694*, 1189–1195. [CrossRef]

28. Liu, J.; Scheerbaum, N.; Lyubina, J.; Gutrleisch, O. Reversibility of magnetostructural transition and associated magnetocaloric effect in Ni-Mn-In-Co. *Appl. Phys. Lett.* **2008**, *93*, 102512. [CrossRef]

29. Jiang, Y.; Li, Z.; Li, Z.; Yang, Y.; Yang, B.; Zhang, Y.; Esling, C.; Zhao, X.; Zuo, L. Magnetostructural transformation and magnetocaloric effect in Mn-Ni-Sn melt-spun ribbons. *Eur. Phys. J. Plus* **2017**, *132*, 42. [CrossRef]